

Development

# Loss of Tiparp Results in Aberrant Layering of the Cerebral Cortex

Giulia Grimaldi,<sup>1\*</sup> Barbora Vagaska,<sup>1\*</sup> Oleksandr Ievglevskiy,<sup>1</sup> Elena Kondratskaya,<sup>1</sup> Joel C. Glover,<sup>1</sup> and Jason Matthews<sup>1,2</sup>

<https://doi.org/10.1523/ENEURO.0239-19.2019>

<sup>1</sup>Institute of Basic Medical Sciences, University of Oslo, Oslo 0372, Norway and <sup>2</sup>Department of Pharmacology and Toxicology, University of Toronto, Toronto, Ontario M5S 1A8, Canada

## Abstract

2,3,7,8-tetrachlorodibenzo-p-dioxin (TCDD)-inducible poly-ADP-ribose polymerase (TIPARP) is an enzyme that adds a single ADP-ribose moiety to itself or other proteins. Tiparp is highly expressed in the brain; however, its function in this organ is unknown. Here, we used *Tiparp*<sup>-/-</sup> mice to determine Tiparp's role in the development of the prefrontal cortex. Loss of Tiparp resulted in an aberrant organization of the mouse cortex, where the upper layers presented increased cell density in the knock-out mice compared with wild type. Tiparp loss predominantly affected the correct distribution and number of GABAergic neurons. Furthermore, neural progenitor cell proliferation was significantly reduced. Neural stem cells (NSCs) derived from *Tiparp*<sup>-/-</sup> mice showed a slower rate of migration. Cytoskeletal components, such as  $\alpha$ -tubulin are key regulators of neuronal differentiation and cortical development.  $\alpha$ -tubulin mono-ADP ribosylation (MAR) levels were reduced in *Tiparp*<sup>-/-</sup> cells, suggesting that Tiparp plays a role in the MAR of  $\alpha$ -tubulin. Despite the mild phenotype presented by *Tiparp*<sup>-/-</sup> mice, our findings reveal an important function for Tiparp and MAR in the correct development of the cortex. Unravelling Tiparp's role in the cortex, could pave the way to a better understanding of a wide spectrum of neurological diseases which are known to have increased expression of TIPARP.

**Key words:** cortex; cortex layering; mono-ADP ribosylation; PARP; post-translational modification; Tiparp

## Significance Statement

2,3,7,8-tetrachlorodibenzo-p-dioxin (TCDD)-inducible poly-ADP-ribose polymerase (TIPARP) is an enzyme which adds a single ADP-ribose moiety to itself or other proteins and is highly expressed in the brain. However, its function in this organ remains unknown. Here, we show that Tiparp affects neural progenitor cell proliferation and migration, and its loss leads to aberrant organization of the mouse cortex, predominantly by disrupting the correct distribution and number of GABAergic neurons. Cytoskeletal components, such as  $\alpha$ -tubulin, are key regulators of neuronal differentiation and cortical development, here, we show that Tiparp is part of a complex that interacts with  $\alpha$ -tubulin and plays a role in its mono-ADP ribosylation (MAR). Despite the mild phenotype presented by the *Tiparp* knock-out mouse our findings reveal an important function of MAR by this enzyme in the correct development of the cortex.

## Introduction

2,3,7,8-tetrachlorodibenzo-p-dioxin (TCDD)-inducible poly-ADP-ribose polymerase (TIPARP; also known as, PARP7/ARTD14/RM1) is expressed in many different tis-

ues, including liver, heart, spleen, brain, and reproductive organs (Ma et al., 2001). TIPARP is one of 17 members of the PARP family that have diverse cellular

Received June 17, 2019; accepted October 10, 2019; First published November 8, 2019.

The authors declare no competing financial interests.

Author contributions: G.G. and B.V. designed research; G.G., B.V., O.I., and E.K. performed research; G.G., B.V., and J.M. analyzed data; G.G. and J.M. wrote the paper; J.G. and J.M. contributed unpublished reagents/analytic tools.

functions but share a conserved catalytic PARP domain. They use nicotinamide adenine dinucleotide (NAD<sup>+</sup>) as a substrate to transfer one or more molecules of ADP-ribose to specific amino acid residues on target proteins. TIPARP mono-ADP-ribosylates itself and other proteins including, TANK-binding protein 1 (TBK1) and the aryl hydrocarbon receptor (AHR; MacPherson et al., 2013; Ahmed et al., 2015). TIPARP regulates the pluripotency of embryonic stem cells, mediates Type I interferon-dependent antiviral responses, regulates autophagy and acts as a transcriptional repressor (MacPherson et al., 2013; Roper et al., 2014; Yamada et al., 2016; Han et al., 2018). It contains an N-terminus, followed by a CCCH-zinc finger domain, a WWE (tryptophan–tryptophan–glutamate) domain, and the conserved PARP catalytic domain. Within the N-terminus there is a short nuclear localization sequence which, along with the zinc finger domain, ensures that TIPARP is predominantly found in the nucleus; however, localization of TIPARP varies among cell lines and during different stages of the cell cycle (Vyas et al., 2013; Gomez et al., 2018). In HeLa cells, TIPARP has a diffuse cytoplasmic localization during mitosis, but it forms nuclear foci during interphase (Vyas et al., 2013). Moreover, in response to viral infection, reactive oxygen species (ROS), and mitochondrial damage, TIPARP translocates from the nucleus to the cytosol (Kozaki et al., 2017).

AHR is a ligand responsive transcription factor predominantly studied for its ability to mediate toxic responses of environmental pollutants, such as TCDD (Fernandez-Salguero et al., 1996). However, it is activated by numerous endogenous ligands and plays important roles in immune function, inflammation, stem cell differentiation, neurologic development and behavior (Stockinger et al., 2014). It has previously been reported that TIPARP functions as part of a negative feedback loop regulating AHR activity and that *Tiparp*<sup>-/-</sup> mice exhibit an increased sensitivity to dioxin-induced toxicities primarily due to increased AHR activity (Hutin et al., 2018).

The effects of TCDD and AHR in neurons, brain and cognitive functions has been investigated in numerous studies (Powers et al., 2005; Hood et al., 2006; Nishijo et al., 2007; Collins et al., 2008; Lin et al., 2008; Kimura et al., 2017). TCDD exposure in rodents has been reported to perturb the dendritic morphology of neurons (Kimura et al., 2015), cortical layer formation (Mitsuhashi et al., 2010), and neurogenesis in cerebellar granule cells (Collins et al., 2008). Treated rodents also exhibit a distinct

decrease in behavioral flexibility, associate learning, memory, neuronal response to stimuli, locomotor activity and social behavior as well as increased anxiety. The majority of these effects are mediated by AHR, which has an important role in regulating developmental processes required for higher brain function in adulthood (Kimura and Tohyama, 2017). Recently, TCDD treatment was reported to promote migration of astrocytes in an Ahr-dependent manner and affect GABAergic neurons resulting in their altered distribution in the medial prefrontal cortex, although the mechanism of action remains elusive (Nguyen et al., 2013; Chen et al., 2019). In *Caenorhabditis elegans*, *ahr-1*, the orthologue of AHR, is implicated in specifying GABAergic neuron cell fate (Huang et al., 2004).

In humans, children exposed to TCDD and TCDD-like environmental pollutants before birth have impaired higher cognitive functions, which is supported by another report linking exposure to AHR activating poly aromatic hydrocarbons with intelligence in children (Seegal, 1996; Perera et al., 2009).

Increased *Tiparp* expression was observed in rat brains during the developmental formation of the neural network and during long-term potentiation (LTP) in adults (Matsuo et al., 2000). This suggests that TIPARP functions in brain development and in neuronal plasticity in adulthood, and may represent a key enzyme involved in molecular cascades that lead to structural changes in synaptic connections. Moreover, TIPARP was identified as a highly upregulated protein following trace fear conditioning and in neurologic disorders, such as epilepsy (Steenland, 2010; Dachet et al., 2015). In an integrated multi-cohort transcriptional meta-analysis of neurodegenerative diseases, TIPARP was shown to be strongly upregulated independently of age (Li et al., 2014). Despite several reports identifying the *TIPARP* gene or its product as being elevated in neuronal diseases, there are no studies that investigate the physiologic role of *Tiparp* in the brain. Unravelling its potential role in the brain could pave the way to better understanding a wide spectrum of neurologic diseases. Herein, we investigated the effects of loss of *Tiparp* in the mouse cortex.

## Materials and Methods

### Animals

All experiments were approved by the Norwegian Animal Research authority (FOTS ID 10420). Mice were housed in a 12/12 h light/dark cycle and had access to food and water *ad libitum*. The *Tiparp*<sup>-/-</sup> mice where exon 3 of the *Tiparp* gene was removed were generated in C57BL/6N strain. A full description of the generation of these mice has been previously described (Hutin et al., 2018b). The animal colony was maintained by breeding heterozygotes and thus strain-specific wild-type (*Tiparp*<sup>+/+</sup>) control mice or *Tiparp*<sup>-/-</sup> mice were used in all experiments. Mice of either sex and wherever possible same sex littermates were used in these studies.

This work was supported by the European Union Seventh Framework Program (FP7-PEOPLE-2013-COFUND) Grant n609020-Scientia Fellows (to G.G.) and by the Johan Throne Holst Foundation and the University of Oslo (J.M.).

\*G.G. and B.V. contributed equally to this work.

Correspondence should be addressed to Jason Matthews at [jason.matthews@medisin.uio.no](mailto:jason.matthews@medisin.uio.no) or Giulia Grimaldi at [giulia.grimaldi@medisin.uio.no](mailto:giulia.grimaldi@medisin.uio.no).

<https://doi.org/10.1523/ENEURO.0239-19.2019>

Copyright © 2019 Grimaldi et al.

This is an open-access article distributed under the terms of the Creative Commons Attribution 4.0 International license, which permits unrestricted use, distribution and reproduction in any medium provided that the original work is properly attributed.

**Table 1. Primer sequences of the primers used for qPCR**

Gene name	Forward primer sequence	Reverse primer sequence
<i>Blbp</i>	GGACACAATGCACATTCAAGAAC	CCGAACCACAGACTTACAGTTT
<i>Cyp1a1</i>	CGTTATGACCATGATGACCAAGA	TCCCAAACACTCATTGCTCAGAT
<i>Dcx</i>	CCTTGATGGAAAGCAGGTCAC	GGCCTGGGCTTTTAGCAGAT
<i>Gfap</i>	CAGATCCGAGGGGGCAAAG	TGGCAGGGCTCCATTTTCAA
<i>Glast1</i>	ACCAAAAGCAACGGAGAAGAG	GGCATTCCGAAACAGGTAACCT
<i>Nestin</i>	CCCTGAAGTCGAGGAGCTG	CTGCTGCACCTCTAAGCGA
<i>Nfh</i>	GCCGCTTACAGAAAGCTCCT	ATGTGCGTGGATATGGAGGG
<i>Ng2</i>	GGGCTGTGCTGTCTGTTGA	TGATTCCCTTCAGGTAAGGCA
<i>Olig1</i>	TCTTCCACCGCATCCCTTCT	CCGAGTAGGGTAGGATAACTTCG
<i>Pax6</i>	TACCAGTGTCTACCAGCCAAT	TGCACGAGTATGAGGAGGTCT
<i>Pdgfr</i>	AGAGTTACACGTTTGAGCTGTG	GTCCCTCCACGGTACTCCT
<i>Sox2</i>	ACAGAGAAAACCTGAGGGCG	GAAGCGCCTAACGTACCACT
<i>TBP</i>	GCACAGGAGCCAAGAGTGAA	TAGCTGGGAAGCCCCAACTTC
<i>Tiparp</i>	ACATCACACCGTATTGCCCT	GCCCAAAGTCTTGTCTCCTCCAT
<i>Tubb3</i>	TGAGGCCTCCTCTACAAGTA	CCGCACGACATCTAGGACTG

### RNA isolation and qPCR

Mice were euthanized by open-drop exposure to isoflurane and cervical dislocation. The brains were extracted in ice-cold PBS, various brain regions were dissected and flash frozen in liquid nitrogen. The tissue was then homogenized in TRIzol reagent (Thermo Fisher Scientific) and total RNA and RNA from mouse neural stem cells (mNSCs) were isolated with Aurum Total RNA Mini kit (Bio-Rad) according to the manufacturer's instructions. All RNA was reverse transcribed using High-Capacity cDNA Reverse Transcription kit (Thermo Fisher Scientific). Transcript levels were quantified by qPCR using KAPA SYBR Fast Universal kit (Sigma-Aldrich). The amplified genes were normalized to tata-binding protein (*Tbp*). Primer sequences are provided in Table 1.

### Immunohistochemistry

Mice were euthanized as described above and the brains were dissected in ice-cold PBS and then fixed overnight in 4% paraformaldehyde (PFA). Fixed brains were washed with PBS and incubated overnight in 30% (w/v) sucrose before embedding in Optimal Cutting Temperature compound (OCT). All mouse brain tissue was cryo-sectioned into 15- $\mu$ m-thick sections, which were air dried before use. Unless noted otherwise, sagittal section from comparable lateral regions within a third from the midline were used.

For Nissl staining, sections were placed in 0.1% cresyl violet solution for 10 min at 37° before rinsing them in distilled water and then differentiated in 95% ethyl alcohol for 15 min. The sections were then dehydrated in 100% alcohol twice for 5 min. The sections were cleared in xylene twice for 5 min before mounting.

mNSCs were grown on poly-D-lysine coated glass cover slips, whereas COS-1 cells were grown on non-coated cover slips. Both cell types were fixed for 15 min in 4% PFA before proceeding with immunofluorescence staining.

For immunofluorescence sections or cells were rinsed in PBS then blocked for 45 min in 0.1% Triton X-100, 10% BSA in PBS at room temperature. Sections were then incubated overnight at 4°C with primary antibodies. They were washed in PBS and incubated at room tem-

perature for 1 h with species-appropriate Alexa Fluor or cyanine dye conjugated secondary antibodies and Hoechst 33258 (Sigma) and mounted with Vectashield anti-fading mounting medium (Vectorlabs). The antibodies used are provided in Table 2. Images were obtained with a Zeiss LSM 710 confocal or Zeiss Axio Observer microscope. Immunohistochemistry images were analyzed with CellProfiler 3.0 software ([www.cellprofiler.org](http://www.cellprofiler.org); Broad Institute; Carpenter et al., 2006) and bin analysis, where the thickness of the cortex was divided into 40 equal intervals, was done with KNIME Analytics Platform ([www.knime.com](http://www.knime.com); Berthold et al., 2009)

### Electrophysiology

For whole-cell patch-clamp experiments, mice (P14–P21) were euthanized as described above, and the brain rapidly removed to ice-cold oxygenated (95% O<sub>2</sub>/5% CO<sub>2</sub>) artificial CSF (ACSF; 128 mM NaCl, 4 mM KCl, 21 mM NaHCO<sub>3</sub>, 0.5 mM NaH<sub>2</sub>PO<sub>4</sub>, 30 mM glucose, 1 mM MgCl<sub>2</sub>, and 1 mM CaCl<sub>2</sub>; pH 7.2; 290–300 mOsm/l). Coronal brain slices of 350  $\mu$ m containing the cerebral cortex at the emergence of the dorsal hippocampus were cut using a vibrating microtome (VT1000S; Leica). Slices were stored and allowed to recover at room temperature in a submerged chamber in oxygenated standard ACSF (same composition as dissection ACSF, except that CaCl<sub>2</sub> was at a concentration of 2 mM) for at least 1 h before experimentation. The slices were then transferred to a submersion chamber that was perfused with the oxygenated ACSF at 31°C for whole-cell recording. The cortex primary neurons were visually identified by their pyramidal shape and regular spikes with an up-right infrared-differential interference contrast (IR-DIC) microscope (Olympus BX51WI) and captured with a CoolSNAP EZ with SSD ICX285 (Photometrics) video camera. Spontaneous IPSCs and EPSCs were recorded by using patch clamp technique in a whole-cell configuration. Patch electrodes were fabricated from borosilicate glass capillaries with an outer diameter of 1.5 mm (Sutter Instruments) using an automated puller (PC-10; Narishige). The internal pipette solution for studying excitatory synapses contained 130 mM K-methylsulfate, 5 mM NaCl, 1 mM CaCl<sub>2</sub>, 20 mM HEPES, 0.5 mM EGTA, 3 mM Mg-ATP, and 0.4

**Table 2. List of primary and secondary antibodies used**

Antibody	RR ID	Target antigen	Manufacturer	Catalog number	Host	Clone	Dilution
GFP	<a href="#">AB_300798</a>	GFP	Abcam	ab13970	chicken	polyclonal	1:3000 (IHC)
GFP	<a href="#">AB_303395</a>	GFP	Abcam	ab290	rabbit	polyclonal	1:1000 (WB)
Parvalbumin	<a href="#">AB_2174013</a>	Ca <sup>+2</sup> -binding site/ specifically stains the Ca <sup>+2</sup> -bound form of parvalbumin	Millipore	MAB1572	mouse	monoclonal, IgG1, clone PARV-19	1:500 (IHC)
Calbindin	<a href="#">AB_10000340</a>	Calbindin D-28k	Swant	CB 38	rabbit	polyclonal	1:1000 (IHC)
Calretinin	<a href="#">AB_10000321</a>	Calretinin human	Swant	7699/3H	rabbit	polyclonal	1:200 (IHC)
NeuN-biotin conjugated	<a href="#">AB_2298772</a>	Neuron-specific nuclear protein/ FOX3/RBFOX3	Millipore	MAB377B	mouse	monoclonal IgG1, clone A60	1:500 (IHC)
Biotinylated Wisteria Floribunda agglutinin (WFA)	N/A	N-acetylgalactosamine (GalNAc)	Sigma	L1766	N/A	N/A	1:100 (IHC)
GFAP	<a href="#">AB_10013382</a>	Glial fibrillary acidic protein	Dako	Z0334	rabbit	polyclonal	1:400 (IHC)
TUBB3	<a href="#">AB_262133</a>	Tubulin, $\beta$ III	Sigma	T2200	rabbit	polyclonal	1:500 (IHC)
SOX2	N/A	Transcription factor SOX-2	Stem Cell Tech	60055	rabbit	polyclonal	1:100 (IHC)
Nestin/radial glial marker	<a href="#">AB_531887</a>	Nestin	DSHB	RC2	mouse	monoclonal, IgM	1:10 (IHC)
Vimentin	<a href="#">AB_531888</a>	Vimentin	DSHB	3CB2	mouse	monoclonal, IgM	1:10 (IHC)
Pax6	<a href="#">AB_291612</a>	Pax6	Covance Research Products	PRB-278P	rabbit	polyclonal	1:100 (IHC)
Pax6	<a href="#">AB_528427</a>	Pax6	DSHB	PAX6	mouse	monoclonal IgG1	1:10 (IHC)
CNP/Rip	<a href="#">AB_531796</a>	2',3'-cyclic- nucleotide 3'-phosphodiesterase (CNP)	DSHB	Rip	mouse	monoclonal, IgG1	1:100 (IHC)
Synapsin ½	<a href="#">AB_1106784</a>	Synapsin 1/2	Synaptic Systems	106 004	guinea pig	polyclonal	1:200 (IHC)
Ctip2	<a href="#">AB_2064130</a>	BCL11B	Abcam	ab18465	rat	polyclonal	1:500 (IHC)
Satb2	<a href="#">AB_882455</a>	SATB2	Abcam	ab51502	mouse	monoclonal, IgG1	1:200 (IHC)
$\alpha$ -Tubulin	<a href="#">AB_477579</a>	$\alpha$ -Tubulin	Sigma	T5168	mouse	monoclonal, IgG1, clone B-5-1-2	1:500 (IHC), 1:10000 (WB), 2.5 $\mu$ g/rxn (IP)
$\beta$ -Actin	<a href="#">AB_476697</a>	b-actin	Sigma	A2228	mouse	monoclonal, IgG1, clone AC-74	1:10000 (WB)
pH3	<a href="#">AB_310177</a>	Phospho-histone H3 (Ser10)	Millipore	06-570	rabbit	polyclonal	1:500 (IHC)
Acetylated $\alpha$ -tubulin	<a href="#">AB_477585</a>	$\alpha$ -Tubulin, acetylated (Lys-40)	Sigma	T6793	mouse	monoclonal, IgG2b, clone 6-11B-1	1:1000 (WB)
Anti-mono-ADP- ribose binding reagent	<a href="#">AB_2665469</a>	Mono ADP-ribose	Millipore	MABE1076	E.coli	monoclonal	1:1000 (WB)
Secondary antibody	RR ID	Conjugated	Manufacturer	Catalog number	Host		
Anti-mouse IgG	<a href="#">AB_330924</a>	HRP	Cell Signaling	7076S	horse		
Anti-rabbit IgG	<a href="#">AB_2099233</a>	HRP	Cell Signaling	7074S	goat		
Anti-chicken IgY	<a href="#">AB_2534096</a>	Alexa Fluor 488	Thermo Fisher	A11039	goat		
Anti-guinea Pig	<a href="#">AB_2337438</a>	Alexa Fluor 488	Jackson ImmunoResearch	106-545-003	goat		
Anti-mouse IgG	<a href="#">AB_2338685</a>	Cy3	Jackson ImmunoResearch	115-165-062	goat		
Anti-Mouse IgG	<a href="#">AB_2340846</a>	Alexa Fluor 488	Jackson ImmunoResearch	715-545-150	donkey		
Anti-mouse IgM, $\mu$ chain specific	<a href="#">AB_2340844</a>	Alexa Fluor 488	Jackson ImmunoResearch	715-546-020	donkey		
Anti-rabbit IgG	<a href="#">AB_2307443</a>	Cy3	Jackson ImmunoResearch	711-165-152	donkey		
Anti-rabbit IgG	<a href="#">AB_143165</a>	Alexa Fluor 488	Thermo Fisher	A11008	goat		
Anti-rat IgG	<a href="#">AB_2535794</a>	Alexa Fluor 488	Thermo Fisher	A-21208	donkey		
Streptavidin	<a href="#">AB_2337246</a>	Cy2	Jackson ImmunoResearch	016-220-084			
Streptavidin	<a href="#">AB_2337244</a>	Cy3	Jackson ImmunoResearch	016-160-084			

mM Na<sub>3</sub>GTP-GTP (Devlin et al., 2015). The solution for studying inhibitory synapses was composed of 135 mM Cs-MeSO<sub>4</sub>, 10 mM CsCl, 10 mM HEPES, 0.5 mM EGTA, and 4 mM Mg-ATP. Pipette solutions were freshly made and filtered (0.1 μm), osmolarity was 295–305 mOsmol, and pipette resistance was 5–7 MΩ.

To separate IPSCs and EPSCs (typically throughout the entire experiment), different holding potentials were applied ( $V_h = 0$  and  $V_h = -60$  or  $-70$  for IPSCs and EPSCs, respectively). All recordings were performed using a MultiClamp 700B amplifier (Molecular Devices). Recordings and pre-processing of data were made with WinWCP (University of Strathclyde). The signals were typically low-pass filtered with a corner frequency ( $-3$  dB) of 3 kHz and sampled at 6 kHz by DigiData 1322A (Molecular Devices).

Data analysis was performed with p-CLAMP 10 (Molecular Devices) and OriginLab 8 (OriginLab Corp.). sPSCs were detected with a threshold of 5–7 pA, depending on the noise level via template-based algorithm and by visual verification. Analyses of the kinetic properties of sPSCs included only well separated (interevent intervals  $>40$  ms), monophasic PSCs which appeared to rise in a monotonic fashion without visible deviation of the rising phase and which decayed exponentially. The rise and decay time courses of individual PSCs were estimated by curve fitting with the exponential function:

$$A(t) = A_0 e^{-\frac{t}{\tau}},$$

where  $A(t)$  is the current as a function of time,  $A_0$  is the maximum amplitude of the event (determined as the maximum current of the selected event/response),  $\tau$  is the time constant,  $\tau_{\text{RISE}}$  for event's rise phase and  $\tau_{\text{DECAY}}$  for decay phase

### Differentiation of mNSCs line

Primary mNSC lines isolated from dissected forebrain of E14.5 embryos from *Tiparp*<sup>+/+</sup> and *Tiparp*<sup>-/-</sup> mice were established and cultured as described previously (Pollard, 2013). In brief, the forebrain was dissected out in dissection solution (137 mM NaCl, 5.4 mM KCl, 0.17 mM Na<sub>2</sub>HPO<sub>4</sub>, and 0.22 mM KH<sub>2</sub>HPO<sub>4</sub>) and the meninges were removed. Each forebrain was kept separately in 1 ml of Accutase and put at 37°C for 30 min and triturated with a pipette half way through the incubation. The cells were then triturated again to obtain an almost a single cell suspension in 1 ml of culture medium [DMEM/F12 supplemented with 1% penicillin/streptomycin (P/S), 2% B27, 10 ng/ml EGF, 10 ng/ml FGF, and 2.5 U/ml heparin] and centrifuged 100 × *g* for 4 min. The pellet was then resuspended in 1 ml of culture medium and the non-digested tissue was left to settle by gravity for about 1 min. Cell suspension was then plated in a well of a 12-well plate. The cells were cultured as a monolayer with laminin. Differentiation of the mNSCs in the three lineages was done as previously described (Conti et al., 2005; Glaser et al., 2007; Pollard, 2013). Briefly, for neuronal differentiation cells were placed in culture medium lacking EGF for a week before changing to complete neurobasal medium (neurobasal medium containing 1% P/S, 2% B27,

and 1% GlutaMAX). Experiments were done after a total of 14 d of differentiation and were maintained in complete neurobasal medium supplemented with 2 ng/ml BDNF (Peprotech). To differentiate the cells into astrocytes they were placed in DMEM containing 1% GlutaMAX, 1% P/S, and 20% fetal bovine serum for 7 d before starting the experiments. Lastly, for oligodendrocyte differentiation cells were cultured for 4 d in DMEM/F12 containing 1% P/S, 2% B27, 10 ng/ml FGF, 2.5 U/ml heparin, 10 ng/ml PDGFAA (Peprotech), and 10 μM forskolin. This is to support the glial precursor stage. To then induce differentiation, growth factors were withdrawn and cells were exposed to 30 μg/ml 3'3'5-triiodo-L-thyronine and 200 μM ascorbic acid (Sigma) for 4 d. All cell culture reagents were purchased from Thermofisher Scientific, unless stated otherwise.

### Cell proliferation and cell death assays

Cell proliferation was assessed by methylene blue colorimetric assay as previously described (Pelletier et al., 1988). In brief, for each cell line and timepoint cells were seeded in five wells of a 96-well plate and fixed with 4% PFA for 15 min at room temperature at the indicated timepoints. They were then gently washed with PBS and incubated with methylene blue solution (1% w/v methylene blue in 0.1 M borate buffer; pH 9) for 30 min at room temperature. The excess dye was washed off with four rinses in 0.01 M borate buffer pH 9. The methylene blue was extracted using a 1:1 v/v of ethanol: 0.1 M HCl. The optical density was read at 650 nm with a SynergyH1 microplate reader.

Cell death was assessed by adding 1 μg/ml Hoechst 33258 to the cell culture media for 1.5 h and then adding 5 μg/ml propidium iodine and incubating for a further 30 min. The cells were then imaged with a Zeiss Axio Observer microscope and the ratio of live to dead cells calculated with CellProfiler 3.0 software ([www.cellprofiler.org](http://www.cellprofiler.org); Broad Institute; Carpenter et al., 2006).

Cell migration was assessed by a scratch assay modified from a previous study (Liang et al., 2007). For each cell line and timepoint, five wells of a 24-well plate each containing custom made 1 × 5 × 1 mm silicon inserts. Once the cells were confluent the insert was removed and the cells were placed back into an incubator. At the various timepoints the cells were fixed for 15 min at room temperature with 4% PFA and rinsed with PBS. The scratch was imaged with a Zeiss Axio Observer microscope by phase contrast. The images were then analyzed using the Fiji software (<https://fiji.sc/>; Schindelin et al., 2012).

### Cell-cycle analysis

Cell-cycle analysis was performed by DNA staining of cells followed by flow cytometry. Approximately one million cells per mNSCs line were resuspended by adding 1-ml methanol at  $-20^\circ\text{C}$  drop by drop while vortexing. Cells were incubated for at least 1 h at  $-20^\circ\text{C}$ , then 3 ml of PBS were added, and the cells were spun at 200 × *g* for 3 min. The cell pellet was resuspended in 500 μl of PBS containing 1.5 mg/ml of Hoechst 33258. After 30 min, the cells were strained and analyzed by flow cytometry.

## Immunoprecipitation

Mono-ADP-ribosylation (MAR) of  $\alpha$ -tubulin was verified by immunoprecipitation as previously described (Hutin et al., 2018a). In brief, mNSCs were harvested and the cell pellet was lysed in cell lysis buffer mNSCs (200 mM NaCl, 1% NP40, and 20 mM HEPES at pH 7.4, supplemented with protease inhibitor cocktail; Sigma). Lysates were clarified by centrifugation and the supernatant was incubated for 2 h with anti- $\alpha$ -tubulin (Sigma) antibody and protein G Dynal beads (Thermo Fisher). The bead-antibody-protein complex was then washed three times for 5 min in wash buffer (200 mM NaCl, 0.1% NP40, and 20 mM HEPES at pH 7.4, supplemented with protease inhibitor cocktail; Sigma). The proteins were then eluted from the beads with  $2\times$  Laemmli buffer and separated by SDS-PAGE and transferred to PVDF membranes. Membranes were probed with anti-mono-ADP-ribose-binding reagent (Millipore) followed by incubation with the appropriate secondary antibody. A list of all antibodies is provided in Table 2.

COS-1 cells were transfected with 2  $\mu$ g of EGFP, GFP-Tiparp, or GFP-Tiparp<sup>H532A</sup> plasmids (MacPherson et al., 2013) per well of a six-well plate using Lipofectamine 2000 reagent according to the manufacturer's instructions. The next morning, cells were harvested, protein extracts were made and the immunoprecipitation was conducted as described above.

## Statistical analyses

All data were presented as means and SEM. A two-tailed Mann-Whitney *post hoc*, a Kruskal-Wallis one-way ANOVA test followed by a Dunn's multiple comparison, a two-way ANOVA test or Student's *t* test were used to assess statistical significance ( $p < 0.05$ ). *U* values for the Mann-Whitney test are reported in the Extended Data Figures 1-1, 4-1, 5-1.

## Results

Tiparp mRNA expression levels were analyzed in the cortex, hippocampus, cerebellum and midbrain of two- to four-month-old C57BL/6N mice, as well as in the liver for comparison. High mRNA levels were observed in the cortex and hippocampus compared with the liver (~4 and 3.8 times higher than in liver, respectively) as well as in the brainstem, which included the diencephalon, and the cerebellum, albeit at lower levels (2.5 and 2 times higher than in liver, respectively; Fig. 1A). To establish the role of Tiparp in the brain, we performed histologic analysis on the cerebral cortex of *Tiparp*<sup>-/-</sup> and *Tiparp*<sup>+/+</sup> mice at two to four months of age. The distribution of cells along the thickness of the cortex was analyzed by determining the *y*-position of each Nissl-stained cell in comparable sagittal brain sections followed by data binning. *Tiparp*<sup>-/-</sup> mice had a significantly higher percentage of cells in the upper layers of the cortex compared with the lower ones (Fig. 1B). Neuronal-specific NeuN staining suggested that the aberrant distribution of cells along the height of the cortex was due to mislocalization of neurons. *Tiparp*<sup>-/-</sup> mice had significantly more NeuN-positive cells in the upper layers at the expense of the lower ones compared with *Tiparp*<sup>+/+</sup> mice (Fig. 1C). Despite the differences in the

cell distribution, they had comparable total cell numbers throughout the thickness of the cortex (Fig. 1B,C, lower panels).

The majority of the differences in cell distribution along the thickness of the cortex were observed around bins 5–15 (Fig. 1A,B). Because of this observation, we then investigated whether this aberrant organization of the neurons along the cortex was due to impaired migration of the neurons from the deep layers to the upper layers during development. Thus, we analyzed the expression of a specific Layer V marker, *Ctip2* (Chen et al., 2008). The cortex of *Tiparp*<sup>-/-</sup> mice had significantly less *Ctip2*-positive cells in the middle of the cortex (bins 15–20), but more in the lower third of the cortex compared with *Tiparp*<sup>+/+</sup> ones (Fig. 1D). To further show disorganization of the cortex we also stained for *Satb2*, which is expressed in all, but predominantly, layers in II–V (Chen et al., 2008; Huang et al., 2013). The cortex of *Tiparp*<sup>+/+</sup> mice had more *Satb2*-positive neurons in bins 15–35 and significantly less in bins 35–40 compared with *Tiparp*<sup>-/-</sup> mice (Fig. 1E). Taken together, these data suggest that the loss of Tiparp causes aberrant positioning of various neuronal subtypes across all layers and the entire thickness.

As TCDD has been previously shown to affect GABAergic neurons and TCDD increases Tiparp expression via Ahr, we investigated whether loss of Tiparp had any effects on GABAergic neurons and their distribution. The majority of these neurons in the cortex can be divided into subtypes based on the differential expression of calcium binding proteins: calbindin, calretinin or parvalbumin (Condé et al., 1994; del Río and DeFelipe, 1996; Gabbott and Bacon, 1996). Sagittal brain sections from *Tiparp*<sup>+/+</sup> and *Tiparp*<sup>-/-</sup> mice were stained for the three calcium binding proteins. *Tiparp*<sup>-/-</sup> mice had significantly lower (29%) calretinin and lower (40%) parvalbumin-positive neurons, but higher calbindin (148%) expressing cells compared with *Tiparp*<sup>+/+</sup> littermates (Fig. 2A,C). Perineuronal nets (PNNs) are extracellular matrix structures that preferentially surround parvalbumin expressing GABAergic neurons (Kosaka and Heizmann, 1989; Härtig et al., 1992). We then investigated if the decrease in parvalbumin expressing neurons correlated with a decreased formation of PNNs. *Tiparp*<sup>-/-</sup> mice had lower number of cells (49%) surrounded by these structures (Fig. 2B,C). However, whether loss of PNNs was due to a direct effect of Tiparp on the extracellular structures or whether this was due to a decrease in parvalbumin-positive neurons remains to be studied. Taken together, these data suggest that Tiparp affects the number and correct distribution of GABAergic neurons in the cortex.

To determine whether Tiparp loss impaired neuronal networks and interfered with the excitability of cortical pyramidal neurons and the alternation of cortical microcircuitry, we did whole-cell patch-clamp recordings. Specifically, we investigated the characteristic current–voltage (*I*-*V*) curves from action potentials to assess the firing rate of pyramidal neurons and assessed the minimal current injection required to trigger enough membrane depolarization for the cells to generate an action potential. Both EPSCs and

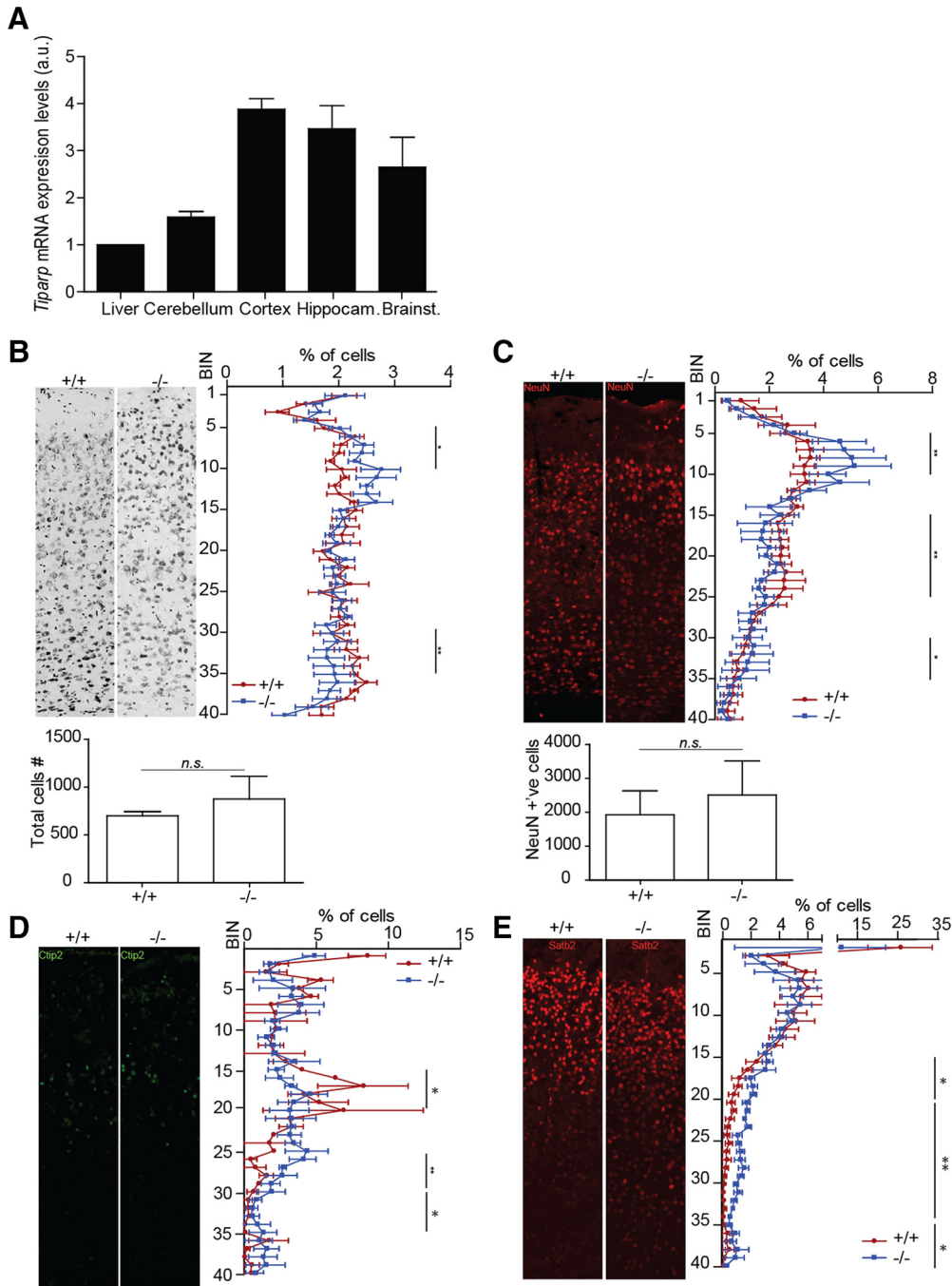


**Figure 1.** *Tiparp* is highly expressed in the adult mouse brain and its depletion leads to aberrant layering. **A**, qPCR of *Tiparp* gene expression levels in cortex, cerebellum, hippocampus (hippocam.) and brainstem (brainst.), which also included the diencephalon relative to liver ( $n = 3$ ). **B–E**, Representative stainings of comparable sagittal sections from *Tiparp*<sup>+/+</sup> and *Tiparp*<sup>-/-</sup> mouse cortex followed by automated counting of cells and distribution analysis along the y-axis of the cortex. Graphs below **B**, **C** show the total number of cells (**B**) and NeuN-positive cells (**C**) in the area analyzed. **B**, Nissl staining in adult mouse ( $n = 5$ ). **C**, Neurons stained with NeuN in the adult mouse ( $n = 3$ ). **D**, *Ctip2* staining of neurons in Layer V in P5 mouse ( $n = 3$ ). **E**, *Satb2* staining predominantly of neurons in Layers II–V in P5 mouse ( $n = 3$ ). Percentage of cells refers to the percentage of cells in a bin relative to the total number of cells in the area analyzed. The asterisk denotes significant differences between the wild type and the knock-out ( $*p < 0.05$  or  $**p < 0.005$ ), within the delimited bin range, according to a two-tailed Mann–Whitney test. *U* values for the Mann–Whitney test can be found in Extended Data Figure 1-1. Non-significance is denoted with n.s. Data are mean  $\pm$  SEM. The *n* number refers to the number of mice in each group, for panels **B–E**, multiple sections of each mouse brain were analyzed, but statistics was done per animal.

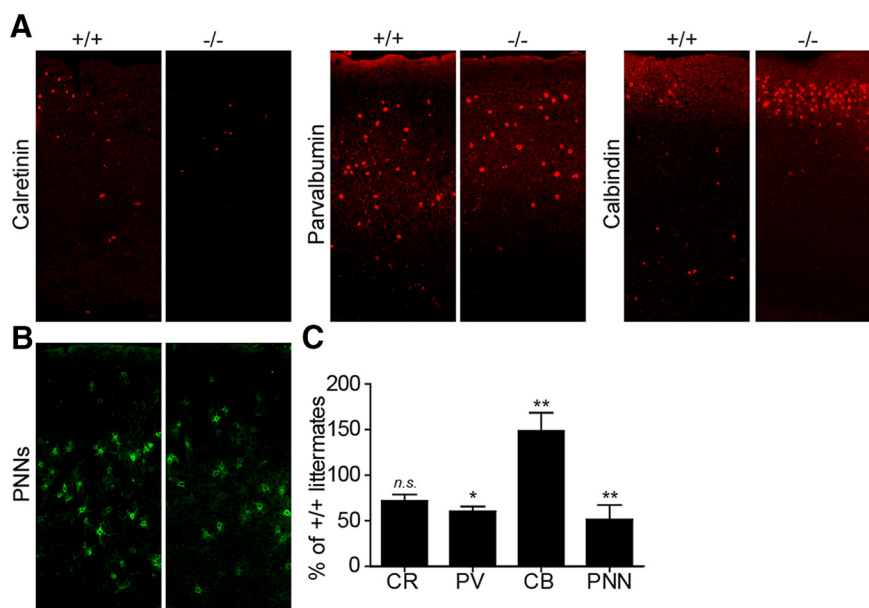


**Figure 2.** *Tiparp*<sup>-/-</sup> mouse cortex presents altered number of GABAergic neurons. **A**, Fluorescent micrographs from representative staining for calretinin (CR), parvalbumin (PV), calbindin (CB), or **B**, perineuronal nets (PNNs) in comparable sagittal sections from *Tiparp*<sup>+/+</sup> and *Tiparp*<sup>-/-</sup> adult mouse cortex. The green fluorescent staining of the PNNs was obtained by biotinylated WFA and Cy2-streptavidin. **C**, Quantification of calretinin, parvalbumin, calbindin expressing cells, and cells surrounded by PNNs, in *Tiparp*<sup>-/-</sup> adult mouse cortex, expressed as percentage of the wild-type littermate ( $n = 3$  mice). Data are mean  $\pm$  SEM. The asterisk denotes significant differences between the wild type and the knock-out (\* $p < 0.05$  or \*\* $p < 0.005$ ) calculated with a two-way ANOVA test. Non-significance is denoted with n.s.

IPSCs were recorded. However, no significant differences were observed in any of these parameters between neurons isolated from *Tiparp*<sup>-/-</sup> and *Tiparp*<sup>+/+</sup> mice (Fig. 3A–F). The resting potential of the cells was also measured and it showed hyperpolarization of *Tiparp*<sup>-/-</sup> neurons compared with those from *Tiparp*<sup>+/+</sup> mice (Fig. 3F), suggesting alterations in function and/or number of ion channels.

To elucidate the developmental mechanisms underlying the aberrant distribution of neurons in the cortex, and to understand whether the observed phenotype was due to aberrant differentiation, proliferation or migration of developing neurons, we isolated mNSCs from both *Tiparp*<sup>+/+</sup> and *Tiparp*<sup>-/-</sup> littermates. Three independent lines were established from two litters. There were no significant differences in the expression of the basic NSC markers at either mRNA level (SOX2, PAX6, Nestin) between genotypes. mNSCs derived from both genotypes expressed comparable protein levels of SOX2 and Nestin (Fig. 4A). Both *Tiparp*<sup>+/+</sup> and *Tiparp*<sup>-/-</sup> mNSCs differentiated into the three neural lineages: neurons, astrocytes and oligodendrocytes. Differentiation into neurons resulted in increased RNA expression levels of the neuronal markers *Tubb3*, *Nfth*, and *Dcx* compared with mNSCs. However, no significant differences in these markers were observed between genotypes (Fig. 4B). Astrocyte differentiation resulted in increased RNA expression levels of astrocyte-specific markers compared with undifferentiated cells (Fig. 4C). Of the three markers examined, we only observed significant increases in *Bilbp* RNA levels between *Tiparp*<sup>-/-</sup> and *Tiparp*<sup>+/+</sup> cells. For oligodendrocyte differentiation, significant increases in *Pdgfra* and

*Ng2* were observed in both genotypes compared with undifferentiated cells. The oligodendrocyte marker, *Ng2*, was significantly increased at the RNA level in *Tiparp*<sup>-/-</sup> compared with *Tiparp*<sup>+/+</sup> cells (Fig. 4D). *Olig1* RNA levels were significantly lower in *Tiparp*<sup>-/-</sup> compared with *Tiparp*<sup>+/+</sup> mNSCs. *Olig1* levels were significantly decreased in differentiation to oligodendrocytes in *Tiparp*<sup>+/+</sup> cells, but unchanged in *Tiparp*<sup>-/-</sup> cells. At protein level, *Tiparp*<sup>-/-</sup> mNSCs differentiated into the three lineages express the typical markers, suggesting that even in the absence of *Tiparp* the cells retain their differentiation potential (Fig. 4B–D). *Tiparp* mRNA levels were significantly downregulated during neuronal cell differentiation, whereas they were significantly upregulated on astrocyte differentiation (Fig. 4E). No changes were observed when cells were differentiated toward the oligodendrocyte lineage (Fig. 4E). This suggested that *Tiparp* expression is regulated during neuronal and astrocytic differentiation and it is involved in the regulation of specific genes involved in differentiation, but it is not a master regulator of neuronal stem cell differentiation.

Next, we assessed the proliferation rate of *Tiparp*<sup>+/+</sup> and *Tiparp*<sup>-/-</sup> mNSCs by conducting a methylene blue assay. Indeed, despite having plated the same number of cells after 72 h, *Tiparp*<sup>-/-</sup> mNSCs had proliferated significantly less than the *Tiparp*<sup>+/+</sup> cells (Fig. 5A). Since no differences in propidium iodine staining were observed between the two genotypes, increases in cell death could not be explained by the slower growth rate of the *Tiparp*<sup>-/-</sup> cells (Fig. 5B). We then stained the cells with Hoechst 33342 and subjected them to flow cytometry to determine the percentage of cells in each phase of the cell-cycle cell.



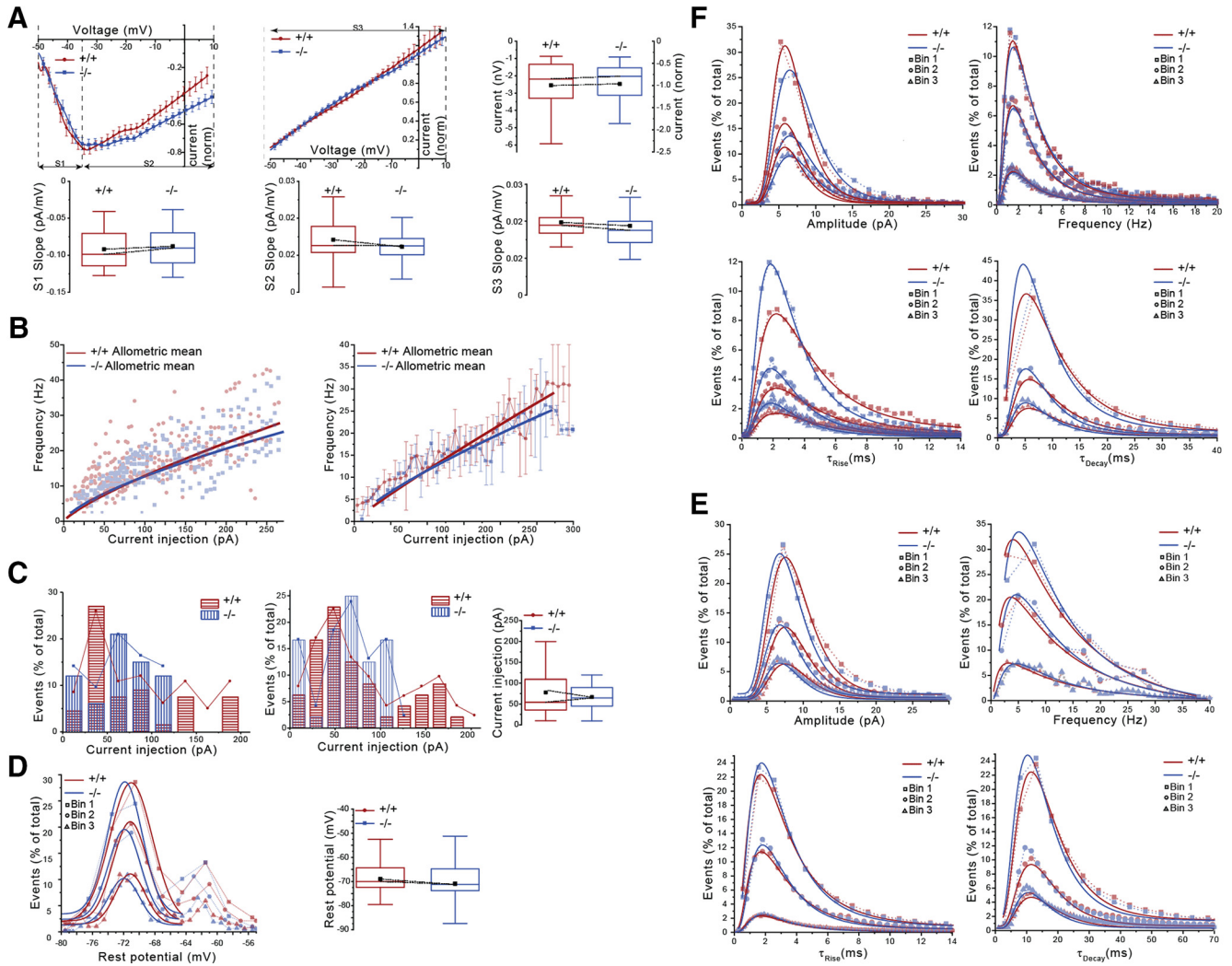


**Figure 3.** Knock-out of *Tiparp* does not affect the electrophysiology of cortex primary neurons. **A**, Characterization of the currents from voltage-clamp recordings show comparable potential dependence of induced currents in the two genotypes. Averaged current–voltage curves (I–V) of inward currents (top left panel) and outward currents (top middle panel) for voltage clamp recordings from whole cells in *Tiparp*<sup>+/+</sup> and *Tiparp*<sup>-/-</sup> adult mouse cortex slices. The top right panel is a box chart representation of the maximum amplitudes of the inward currents. The bottom panel shows box chart representations of the averaged slopes of corresponded periods of the individual IV curves: the inward currents (S1 for the rise and S2 for the decay period; left and middle panel, respectively) and the entire outward currents (slope S3; right panel). These are all calculated for each recording independently. The box represents the data between the second and third quartile, the whiskers represent the range within the 1.5 interquartile range. The black square is the mean and the line within the box is the median value. Current (norm.) is the normalized current expressed in arbitrary units. **B**, Frequencies of action potential firing during step membrane depolarization are similar for *Tiparp*<sup>+/+</sup> and *Tiparp*<sup>-/-</sup> neurons. Concatenated curves (left panel) and the averaged curves of the individual cells (right panel) for depolarization dependent frequencies of action potential firing of *Tiparp*<sup>+/+</sup> and *Tiparp*<sup>-/-</sup> neurons. The allometric function fittings  $f(x) = a \cdot x^b$ , where  $a$  and  $b$  are parameters, were also plotted on the graphs. **C**, Minimal current injection required to trigger enough membrane depolarization for the cells to generate an action potential firing. Distribution curves and histograms of concatenated data of current injections in *Tiparp*<sup>+/+</sup> and *Tiparp*<sup>-/-</sup> cells needed for action potential (AP) generation calculated for bin = 10 pA (left panel) and bin = 20 pA (middle panel) step size. The y-axis represents the fraction of cells depolarized by a given current injection (x-axis) sufficient for AP firing. Most of cells start AP firing when depolarized by a 40- to 80-pA current injection. The right panel is a box plot of the concatenated data that a cell generates an AP under the given minimal current injection. The data does not show normal distribution. **D**, The left panel shows the distribution curves for concatenated data of the resting potential of the patched cells and expressed as the probability to observe a defined resting potential. The graphs represent the Gaussian curves for the data grouped by three different bin sizes. The right panel shows a box chart of the concatenated data of resting potential within the entire data range, the whiskers represent the range within the 1.5 interquartile range. The black square is the mean and the line within the box is the median value. **E, F**, Similarity of functional composition and excitability of *Tiparp*<sup>+/+</sup> and *Tiparp*<sup>-/-</sup> cortical networks: sPSCs. Whole-cell voltage clamp recordings of sIPSCs (**E**) and sEPSCs (**F**) from *Tiparp*<sup>+/+</sup> and *Tiparp*<sup>-/-</sup> adult mouse cortex slices. Concatenated data of the distribution curves for the amplitudes (top left panel); frequencies (top right panel); tau rises (bottom left panel) and tau decays (bottom right panel). The data were grouped into three bins and fitted with lognormal curves.

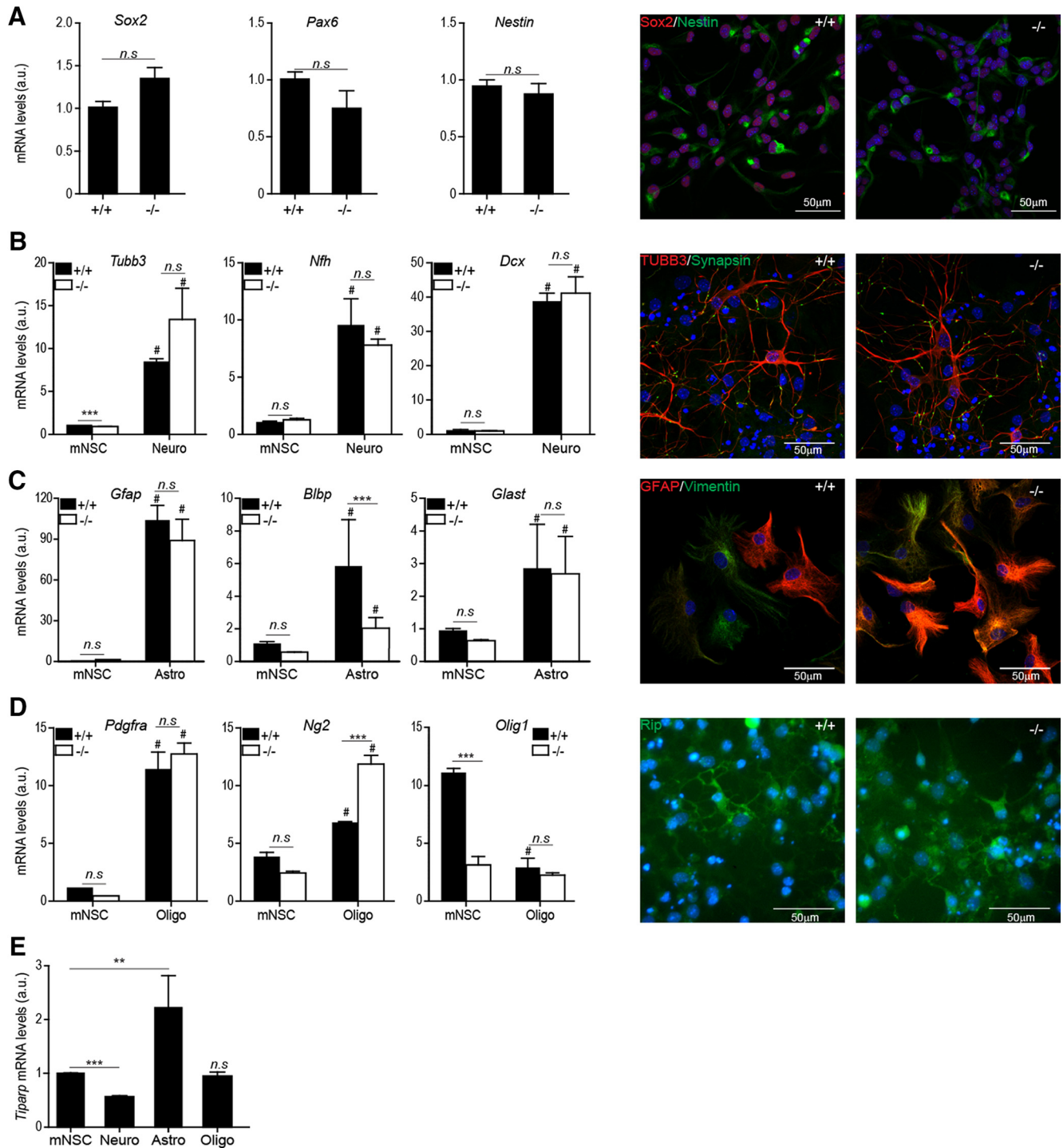


**Figure 4.** Differentiation potential of *Tiparp*<sup>-/-</sup> mNSCs into three lineages. **A–D**, Gene (left panel) and protein (right panel) expression of mNSCs markers in undifferentiated cells (**A**); neuronal markers in cells differentiated toward the neuronal lineage (Neuro) for 14 d (**B**); astrocyte markers in 7-d differentiated astrocytes (Astro; **C**) and oligodendrocyte markers in cells differentiated for 8 d toward the oligodendrocytic lineage (Oligo; **D**). **E**, *Tiparp* gene expression levels in *Tiparp*<sup>+/+</sup> mNSCs and in cells differentiated toward the three neural lineages, as (\*\*\*)  $p < 0.001$  or \*\*  $p < 0.005$ ) between the genotypes determined by a two-tailed Mann–Whitney test (A, E; U values can be found in Extended Data Fig. 4–1) or a two-way ANOVA (**B–D**). Non-significance is denoted by n.s., and # represents statistical significance (at least  $p < 0.05$ ) between undifferentiated and differentiated cells (**B–D**).

The cycle analysis revealed a significantly lower percentage of *Tiparp*<sup>-/-</sup> cells in the S-phase, which was accompanied by a slightly higher percentage of cells in G<sub>0</sub>/G<sub>1</sub>

and G<sub>2</sub>/M phases compared with *Tiparp*<sup>+/+</sup> cells (Fig. 5C). To verify this further, mNSCs in mitosis were analyzed *in vivo* in comparable coronal sections of the prefrontal cor-



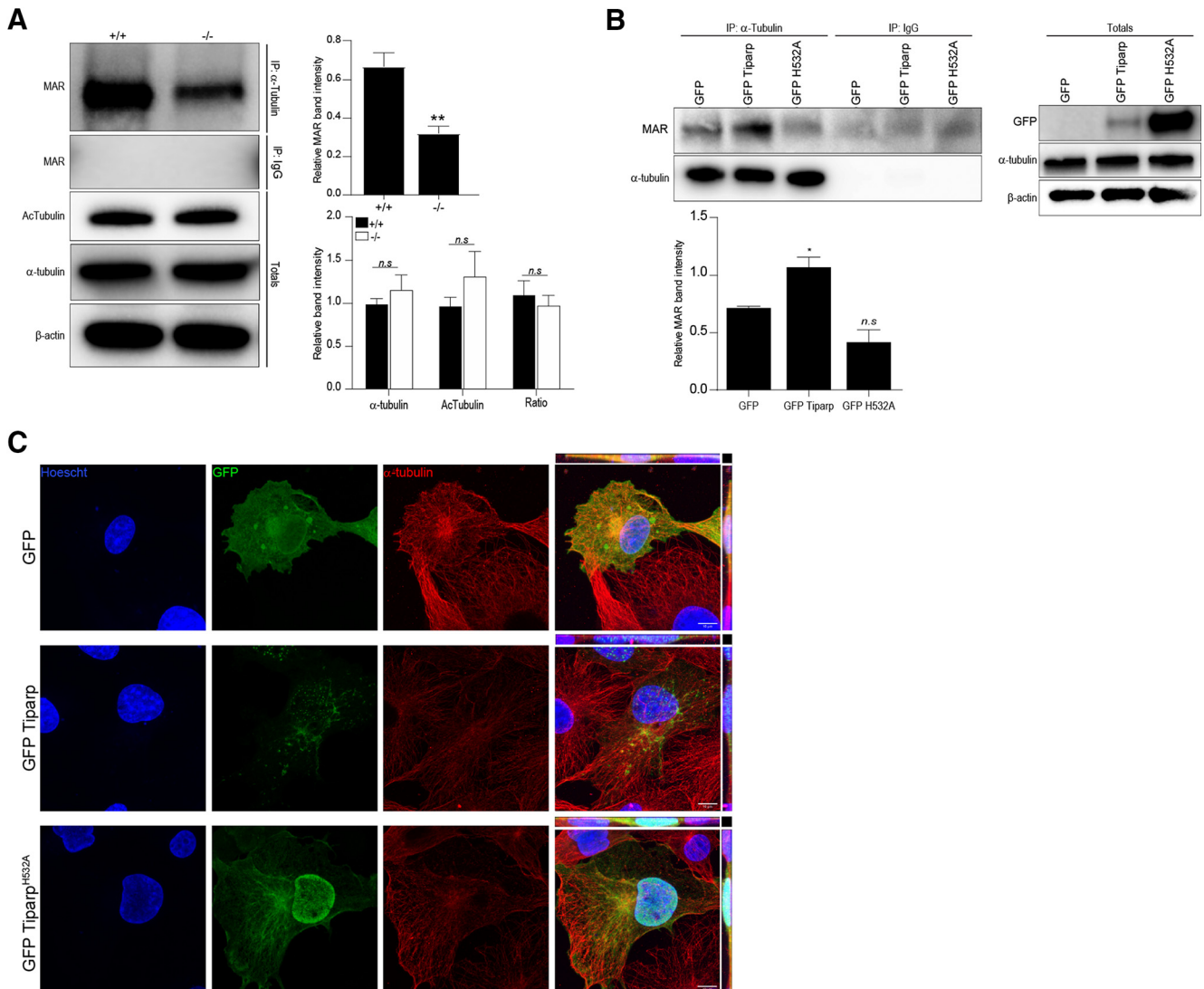


**Figure 6.** Tiparp ADP ribosylates  $\alpha$ -tubulin. **A**, Protein extracts from *Tiparp*<sup>+/+</sup> and *Tiparp*<sup>-/-</sup> mNSCs immunoprecipitation of  $\alpha$ -tubulin followed by western blot against MAR. Total protein extracts were also immunoblotted against acetylated  $\alpha$ -tubulin and  $\alpha$ -tubulin. The right panel shows densitometry analysis of the relative intensity of the MAR band normalized to  $\beta$ -actin (top graph) and relative intensity of the acetylated  $\alpha$ -tubulin,  $\alpha$ -tubulin in the totals normalized to  $\beta$ -actin as well as the acetylated  $\alpha$ -tubulin to  $\alpha$ -tubulin ratio (ratio; bottom panel). **B**, Cell extracts from COS-1 cells overexpressing GFP, GFP-Tiparp or the catalytic mutant GFP-Tiparp<sup>H532A</sup> (labeled GFP-TiparpH532A) were immunoprecipitated with  $\alpha$ -tubulin and immunoblotted against MAR and GFP to show co-precipitation of  $\alpha$ -tubulin and Tiparp. **C**, Cos-1 cells overexpressing GFP, GFP-Tiparp, or GFP-Tiparp<sup>H532A</sup> and stained for  $\alpha$ -tubulin. Data are mean  $\pm$  SEM. The asterisk denotes significant differences between the wild type and the knock-out (\* $p$  < 0.05 and \*\* $p$  < 0.005) calculated with an unpaired  $t$  test (**A**, top panel), a two-way ANOVA (**A**, bottom panel), or an ordinary one-way ANOVA (**B**). Non-significance is denoted by n.s.

activity, since colocalization between  $\alpha$ -tubulin and GFP-Tiparp<sup>H532A</sup> was also observed (Fig. 6C). Taken together, these data suggest that Tiparp plays an important role to MAR of  $\alpha$ -tubulin.

### Discussion

In this study, we demonstrate that Tiparp affects neural progenitor cell proliferation and migration, and its loss leads to aberrant organization of the mouse cortex. Although mild, the phenotype of the *Tiparp*<sup>-/-</sup> mice suggests that alterations in Tiparp expression or function could increase susceptibility to a wide range of both developmental and degenerative neurologic diseases.

We show that *Tiparp*<sup>-/-</sup> mice have less PNNs, which are structures responsible for synaptic stabilization. This observation agrees with a study which used LTP in rats as a cellular model of learning and memory that identified Tiparp as a highly upregulated gene and essential for the maintenance long-lasting LTP, suggesting a close association with plastic changes in the synaptic efficacy. This is achieved by the induction of structural alteration in the synaptic connections and their deep restructuring (Matsuo et al., 2000). However, whether this loss of PNNs is due to the loss of Tiparp is unknown but it does also suggest aberrant synaptic plasticity.

Furthermore, adult *Tiparp*<sup>-/-</sup> mice exhibited atypical laminar organization of the cortex with increased number of cells, and specifically neurons, in the upper layers of the cortex. Reduced staining for specific cortical layer markers was especially evident in Layer V of *Tiparp*<sup>-/-</sup> mice brains. Differentiation and migration of neuronal progenitors during the development of the neocortex is temporally controlled with the migration of cells to specific laminar layers occurring in an inside-out manner. Our findings suggest that Tiparp influences neuronal cell-class determination (layer destination of projection neurons) through regulation of the cell cycle and migration. Furthermore, the *Tiparp*<sup>-/-</sup> mice showed differences of GABAergic neuron distribution with lower amounts of calretinin and parvalbumin-positive interneurons, but higher numbers of calbindin-expressing neurons. The molecular mechanisms underlining this observation remain to be determined.

Ahr influences the migration and differentiation of neurons and specifically of GABAergic neurons (Huang et al., 2004; Qin and Powell-Coffman, 2004). Other studies report that activating the Ahr pathway in mice alters differentiation patterns of neural progenitors and leads to decreased numbers of non-GABAergic projection neurons and thinner deep neocortical layers due to the nuclear accumulation of cyclin-dependent kinase inhibitor p27<sup>Kip1</sup> (Kolluri et al., 1999; Mitsuhashi et al., 2010). Moreover, the absence of Ahr expression compromises GABAergic neuron cell differentiation in the ventral telencephalon (Huang et al., 2004; Gohlke et al., 2009). Tiparp expression is induced by Ahr, which in turn regulates Ahr signaling as part of a negative feedback loop (MacPherson et al., 2013; Grimaldi et al., 2018). Therefore, loss of Tiparp could result in hyperactivation of Ahr signaling, which could partly explain our findings. Alternatively, Tiparp may function in the brain on activation of the Ahr pathway and subsequently target critical proteins in different pathways thus acting as an important downstream regulator of Ahr. Tiparp has been described as both a modulator and cross-pathway mediator of innate immunity. Constitutive Ahr signaling targets Tiparp which in turn mono-ADP ribosylates TBK1, thus suppressing the TBK1-mediated pathway that is essential for interferon induction and the innate immune response (Yamada et al., 2016).

However, Tiparp could also function independently of Ahr. Its expression can be induced by other nuclear receptors important in neuronal development such as glucocorticoid receptor and platelet-derived growth factor receptor (Schmahl et al., 2008; Chinenov et al., 2014). Indeed, *in utero* exposure to synthetic glucocorticoids results in aberrant distribution of neurons throughout the cortex, similar to what we report in this study (Tsiarli, 2014). The complex cytoarchitecture and laminar organization of the cerebral cortex are the result of several processes including neurogenesis, neuronal migration and differentiation. Cortical malformations often show abnormalities in all three processes, because genes involved in one of these processes often affect the other two (Manzini and Walsh, 2011). Cytoskeletal components,

such as  $\alpha$ -tubulin are key regulators of all aspects of neuronal differentiation have been associated with cortical malformations (Francis et al., 2006; Kerjan and Gleeson, 2007; Lian and Sheen, 2015). *Tuba1a* mutant mice have defects associated with cortical Layers II/III and IV and aberrant neuronal migration (Keays et al., 2007). A recent study reported that  $\alpha$ -tubulin is mono-ADP ribosylated; however, the enzyme responsible for this posttranslational modification of  $\alpha$ -tubulin was not reported (Larsen et al., 2018). Here, we provide evidence that Tiparp contributes to the MAR  $\alpha$ -tubulin. Loss of Tiparp expression or its catalytic activity resulted in a significant decrease in mono-ADP-ribosylated  $\alpha$ -tubulin. Since tubulin is regulated by many other mechanisms and other posttranslational modifications, the defects we observed were not as severe as those described in the *Tuba1a* mutant mice (Keays et al., 2007; Kumar et al., 2010; Magiera and Janke, 2014). Collectively, our results suggest that Tiparp plays a role in the development of the cerebral cortex. Further studies are needed to fully characterize its mechanism of action and to dissect the pathways involved in this regulation.

## References

- Ahmed S, Bott D, Gomez A, Tamblin L, Rasheed A, Cho T, MacPherson L, Sugamori KS, Yang Y, Grant DM, Cummins CL, Matthews J (2015) Loss of the mono-ADP-ribosyltransferase, Tiparp, increases sensitivity to dioxin-induced steatohepatitis and lethality. *J Biol Chem* 290:16824–16840.
- Berthold MR, Cebron N, Dill F, Gabriel TR, Kotter T, Meinel T, Ohl P, Thiel K, Wiswedel B (2009) KNIME - the Konstanz information miner: version 2.0 and beyond. *J SIGKDD Explor Newsl* 11:26–31.
- Carpenter AE, Jones TR, Lamprecht MR, Clarke C, Kang IH, Friman O, Guertin DA, Chang JH, Lindquist RA, Moffat J, Golland P, Sabatini DM (2006) CellProfiler: image analysis software for identifying and quantifying cell phenotypes. *Genome Biol* 7:R100.
- Chen B, Wang SS, Hattox AM, Rayburn H, Nelson SB, McConnell SK (2008) The Fezf2-Ctip2 genetic pathway regulates the fate choice of subcortical projection neurons in the developing cerebral cortex. *Proc Natl Acad Sci USA* 105:11382–11387.
- Chen Y, Sha R, Xu L, Xia Y, Liu Y, Li X, Xie HQ, Tang N, Zhao B (2019) 2,3,7,8-Tetrachlorodibenzo-p-dioxin promotes migration ability of primary cultured rat astrocytes via aryl hydrocarbon receptor. *J Environ Sci (China)* 76:368–376.
- Chinenov Y, Coppo M, Gupte R, Sacta MA, Rogatsky I (2014) Glucocorticoid receptor coordinates transcription factor-dominated regulatory network in macrophages. *BMC Genomics* 15:656.
- Collins LL, Williamson MA, Thompson BD, Dever DP, Gasiewicz TA, Opanashuk LA (2008) 2,3,7,8-Tetrachlorodibenzo-p-dioxin exposure disrupts granule neuron precursor maturation in the developing mouse cerebellum. *Toxicol Sci* 103:125–136.
- Condé F, Lund JS, Jacobowitz DM, Baimbridge KG, Lewis DA (1994) Local circuit neurons immunoreactive for calretinin, calbindin D-28k or parvalbumin in monkey prefrontal cortex: distribution and morphology. *J Comp Neurol* 341:95–116.
- Conti L, Pollard SM, Gorba T, Reitano E, Toselli M, Biella G, Sun Y, Sanzone S, Ying QL, Cattaneo E, Smith A (2005) Niche-independent symmetrical self-renewal of a mammalian tissue stem cell. *PLoS Biol* 3:e283.
- Dachet F, Bagla S, Keren-Aviram G, Morton A, Balan K, Saadat L, Valyi-Nagy T, Kupsky W, Song F, Dratz E, Loeb JA (2015) Predicting novel histopathological microlesions in human epileptic brain through transcriptional clustering. *Brain* 138:356–370.

- del Río MR, DeFelipe J (1996) Colocalization of calbindin D-28k, calretinin, and GABA immunoreactivities in neurons of the human temporal cortex. *J Comp Neurol* 369:472–482.
- Devlin AC, Burr K, Borooah S, Foster JD, Cleary EM, Geti I, Vallier L, Shaw CE, Chandran S, Miles GB (2015) Human iPSC-derived motoneurons harbouring TARDBP or C9ORF72 ALS mutations are dysfunctional despite maintaining viability. *Nat Commun* 6:5999.
- Fernandez-Salguero PM, Hilbert DM, Rudikoff S, Ward JM, Gonzalez FJ (1996) Aryl-hydrocarbon receptor-deficient mice are resistant to 2,3,7,8-tetrachlorodibenzo-p-dioxin-induced toxicity. *Toxicol Appl Pharmacol* 140:173–179.
- Francis F, Meyer G, Fallet-Bianco C, Moreno S, Kappeler C, Socorro AC, Tuy FP, Beldjord C, Chelly J (2006) Human disorders of cortical development: from past to present. *Eur J Neurosci* 23:877–893.
- Gabbott PL, Bacon SJ (1996) Local circuit neurons in the medial prefrontal cortex (areas 24a,b,c, 25 and 32) in the monkey: II. Quantitative areal and laminar distributions. *J Comp Neurol* 364:609–636.
- Glaser T, Pollard SM, Smith A, Brüstle O (2007) Tripotential differentiation of adherently expandable neural stem (NS) cells. *PLoS One* 2:e298.
- Gohlke JM, Stockton PS, Sieber S, Foley J, Portier CJ (2009) AhR-mediated gene expression in the developing mouse telencephalon. *Reprod Toxicol* 28:321–328.
- Gomez A, Bindsbøll C, Sathesh SV, Grimaldi G, Hutin D, MacPherson L, Ahmed S, Tamblin L, Cho T, Nebb HI, Moen A, Anonsen JH, Grant DM, Matthews J (2018) Characterization of TCDD-inducible poly-ADP-ribose polymerase (TIPARP/ARTD14) catalytic activity. *Biochem J* 475:3827–3846.
- Grimaldi G, Rajendra S, Matthews J (2018) The aryl hydrocarbon receptor regulates the expression of TIPARP and its cis long non-coding RNA, TIPARP-AS1. *Biochem Biophys Res Commun* 495:2356–2362.
- Han B, Zhang Y, Zhang Y, Bai Y, Chen X, Huang R, Wu F, Leng S, Chao J, Zhang JH, Hu G, Yao H (2018) Novel insight into circular RNA HECTD1 in astrocyte activation via autophagy by targeting MIR142-TIPARP: implications for cerebral ischemic stroke. *Autophagy* 14:1164–1184.
- Hans F, Dimitrov S (2001) Histone H3 phosphorylation and cell division. *Oncogene* 20:3021–3027.
- Härtig W, Brauer K, Brückner G (1992) Wisteria floribunda agglutinin-labelled nets surround parvalbumin-containing neurons. *Neuroreport* 3:869–872.
- Hood DB, Woods L, Brown L, Johnson S, Ebner FF (2006) Gestational 2,3,7,8-tetrachlorodibenzo-p-dioxin exposure effects on sensory cortex function. *Neurotoxicology* 27:1032–1042.
- Huang X, Powell-Coffman JA, Jin Y (2004) The AHR-1 aryl hydrocarbon receptor and its co-factor the AHA-1 aryl hydrocarbon receptor nuclear translocator specify GABAergic neuron cell fate in *C. elegans*. *Development* 131:819–828.
- Huang Y, Song NN, Lan W, Hu L, Su CJ, Ding YQ, Zhang L (2013) Expression of transcription factor Satb2 in adult mouse brain. *Anat Rec (Hoboken)* 296:452–461.
- Hutin D, Grimaldi G, Matthews J (2018a) Methods to study TCDD-inducible poly-ADP-ribose polymerase (TIPARP) mono-ADP-ribosyltransferase activity. *Methods Mol Biol* 1813:109–124.
- Hutin D, Tamblin L, Gomez A, Grimaldi G, Soedling H, Cho T, Ahmed S, Lucas C, Kanduri C, Grant DM, Matthews J (2018b) Hepatocyte-specific deletion of TIPARP, a negative regulator of the aryl hydrocarbon receptor, is sufficient to increase sensitivity to dioxin-induced wasting syndrome. *Toxicol Sci* 165:347–360.
- Keays DA, Tian G, Poirier K, Huang GJ, Siebold C, Cleak J, Oliver PL, Fray M, Harvey RJ, Molnár Z, Piñon MC, Dear N, Valdar W, Brown SD, Davies KE, Rawlins JN, Cowan NJ, Nolan P, Chelly J, Flint J (2007) Mutations in alpha-tubulin cause abnormal neuronal migration in mice and lissencephaly in humans. *Cell* 128:45–57.
- Kerjan G, Gleeson JG (2007) Genetic mechanisms underlying abnormal neuronal migration in classical lissencephaly. *Trends Genet* 23:623–630.
- Kimura E, Tohyama C (2017) Embryonic and postnatal expression of aryl hydrocarbon receptor mRNA in mouse brain. *Front Neuroanat* 11:4.
- Kimura E, Kubo K, Matsuyoshi C, Benner S, Hosokawa M, Endo T, Ling W, Kohda M, Yokoyama K, Nakajima K, Kakeyama M, Tohyama C (2015) Developmental origin of abnormal dendritic growth in the mouse brain induced by in utero disruption of aryl hydrocarbon receptor signaling. *Neurotoxicol Teratol* 52:42–50.
- Kimura E, Kubo KI, Endo T, Ling W, Nakajima K, Kakeyama M, Tohyama C (2017) Impaired dendritic growth and positioning of cortical pyramidal neurons by activation of aryl hydrocarbon receptor signaling in the developing mouse. *PLoS One* 12:e0183497.
- Kolluri SK, Weiss C, Koff A, Göttlicher M (1999) p27(Kip1) induction and inhibition of proliferation by the intracellular Ah receptor in developing thymus and hepatoma cells. *Genes Dev* 13:1742–1753.
- Kosaka T, Heizmann CW (1989) Selective staining of a population of parvalbumin-containing GABAergic neurons in the rat cerebral cortex by lectins with specific affinity for terminal N-acetylgalactosamine. *Brain Res* 483:158–163.
- Kozaki T, Komano J, Kanbayashi D, Takahama M, Misawa T, Satoh T, Takeuchi O, Kawai T, Shimizu S, Matsuura Y, Akira S, Saitoh T (2017) Mitochondrial damage elicits a TCDD-inducible poly(ADP-ribose) polymerase-mediated antiviral response. *Proc Natl Acad Sci USA* 114:2681–2686.
- Kumar RA, Pilz DT, Babatz TD, Cushion TD, Harvey K, Topf M, Yates L, Robb S, Uyanik G, Mancini GM, Rees MI, Harvey RJ, Dobyns WB (2010) TUBA1A mutations cause wide spectrum lissencephaly (smooth brain) and suggest that multiple neuronal migration pathways converge on alpha tubulins. *Hum Mol Genet* 19:2817–2827.
- Larsen SC, Hendriks IA, Lyon D, Jensen LJ, Nielsen ML (2018) Systems-wide analysis of serine ADP-ribosylation reveals widespread occurrence and site-specific overlap with phosphorylation. *Cell Rep* 24:2493–2505.e4.
- Li L, Wei D, Wang Q, Pan J, Liu R, Zhang X, Bao L (2012) MEC-17 deficiency leads to reduced  $\alpha$ -tubulin acetylation and impaired migration of cortical neurons. *J Neurosci* 32:12673–12683.
- Li MD, Burns TC, Morgan AA, Khatri P (2014) Integrated multi-cohort transcriptional meta-analysis of neurodegenerative diseases. *Acta Neuropathol Commun* 2:93.
- Lian G, Sheen VL (2015) Cytoskeletal proteins in cortical development and disease: actin associated proteins in periventricular heterotopia. *Front Cell Neurosci* 9:99.
- Liang CC, Park AY, Guan JL (2007) In vitro scratch assay: a convenient and inexpensive method for analysis of cell migration in vitro. *Nat Protoc* 2:329–333.
- Lin CH, Juan SH, Wang CY, Sun YY, Chou CM, Chang SF, Hu SY, Lee WS, Lee YH (2008) Neuronal activity enhances aryl hydrocarbon receptor-mediated gene expression and dioxin neurotoxicity in cortical neurons. *J Neurochem* 104:1415–1429.
- Ma Q, Baldwin KT, Renzelli AJ, McDaniel A, Dong L (2001) TCDD-inducible poly(ADP-ribose) polymerase: a novel response to 2,3,7,8-tetrachlorodibenzo-p-dioxin. *Biochem Biophys Res Commun* 289:499–506.
- MacPherson L, Tamblin L, Rajendra S, Bralha F, McPherson JP, Matthews J (2013) 2,3,7,8-Tetrachlorodibenzo-p-dioxin poly(ADP-ribose) polymerase (TIPARP, ARTD14) is a mono-ADP-ribosyltransferase and repressor of aryl hydrocarbon receptor transactivation. *Nucleic Acids Res* 41:1604–1621.
- Magiera MM, Janke C (2014) Post-translational modifications of tubulin. *Curr Biol* 24:R351–R354.
- Manzini MC, Walsh CA (2011) What disorders of cortical development tell us about the cortex: one plus one does not always make two. *Curr Opin Genet Dev* 21:333–339.
- Matsuo R, Murayama A, Saitoh Y, Sakaki Y, Inokuchi K (2000) Identification and cataloging of genes induced by long-lasting long-term potentiation in awake rats. *J Neurochem* 74:2239–2249.
- Mitsuhashi T, Yonemoto J, Sone H, Kosuge Y, Kosaki K, Takahashi T (2010) In utero exposure to dioxin causes neocortical dysgenesis

- through the actions of p27Kip1. *Proc Natl Acad Sci USA* 107:16331–16335.
- Nguyen MN, Nishijo M, Nguyen AT, Bor A, Nakamura T, Hori E, Nakagawa H, Ono T, Nishijo H (2013) Effects of maternal exposure to 2,3,7,8-tetrachlorodibenzo-p-dioxin on parvalbumin- and calbindin-immunoreactive neurons in the limbic system and superior colliculus in rat offspring. *Toxicology* 314:125–134.
- Nishijo M, Kuriwaki J, Hori E, Tawara K, Nakagawa H, Nishijo H (2007) Effects of maternal exposure to 2,3,7,8-tetrachlorodibenzo-p-dioxin on fetal brain growth and motor and behavioral development in offspring rats. *Toxicol Lett* 173:41–47.
- Pelletier B, Dhainaut F, Pauly A, Zahnd JP (1988) Evaluation of growth rate in adhering cell cultures using a simple colorimetric method. *J Biochem Biophys Methods* 16:63–73.
- Perera FP, Li Z, Whyatt R, Hoepner L, Wang S, Camann D, Rauh V (2009) Prenatal airborne polycyclic aromatic hydrocarbon exposure and child IQ at age 5 years. *Pediatrics* 124:e195–e202.
- Pollard SM (2013) In vitro expansion of fetal neural progenitors as adherent cell lines. *Methods Mol Biol* 1059:13–24.
- Powers BE, Lin TM, Vanka A, Peterson RE, Juraska JM, Schantz SL (2005) Tetrachlorodibenzo-p-dioxin exposure alters radial arm maze performance and hippocampal morphology in female AhR mice. *Genes Brain Behav* 4:51–59.
- Qin H, Powell-Coffman JA (2004) The *Caenorhabditis elegans* aryl hydrocarbon receptor, AHR-1, regulates neuronal development. *Dev Biol* 270:64–75.
- Roper SJ, Chrysanthou S, Senner CE, Sienerth A, Gnan S, Murray A, Masutani M, Latos P, Hemberger M (2014) ADP-ribosyltransferases Parp1 and Parp7 safeguard pluripotency of ES cells. *Nucleic Acids Res* 42:8914–8927.
- Schindelin J, Arganda-Carreras I, Frise E, Kaynig V, Longair M, Pietzsch T, Preibisch S, Rueden C, Saalfeld S, Schmid B, Tinevez JY, White DJ, Hartenstein V, Eliceiri K, Tomancak P, Cardona A (2012) Fiji: an open-source platform for biological-image analysis. *Nat Methods* 9:676–682.
- Schmahl J, Rizzolo K, Soriano P (2008) The PDGF signaling pathway controls multiple steroid-producing lineages. *Genes Dev* 22:3255–3267.
- Seegal RF (1996) Epidemiological and laboratory evidence of PCB-induced neurotoxicity. *Crit Rev Toxicol* 26:709–737.
- Steenland HW (2010) Mouse medial-prefrontal cortex involvement in trace fear memory during wakefulness and sleep. PhD thesis, University of Toronto.
- Stockinger B, Meglio PD, Gialitakis M, Duarte JH (2014) The aryl hydrocarbon receptor: multitasking in the immune system. *Annu Rev Immunol* 32:403–432.
- Tsiarli MA (2014) Dissecting the role of the glucocorticoid receptor in embryonic cortical development: insights from in utero glucocorticoid exposure. PhD thesis, University of Pittsburgh.
- Vyas S, Chesarone-Cataldo M, Todorova T, Huang YH, Chang P (2013) A systematic analysis of the PARP protein family identifies new functions critical for cell physiology. *Nat Commun* 4:2240.
- Yamada T, Horimoto H, Kameyama T, Hayakawa S, Yamato H, Dazai M, Takada A, Kida H, Bott D, Zhou AC, Hutin D, Watts TH, Asaka M, Matthews J, Takaoka A (2016) Constitutive aryl hydrocarbon receptor signaling constrains type I interferon-mediated antiviral innate defense. *Nat Immunol* 17:687–694.